CHALMERS
UNIVERSITY OF TECHNOLOGY

On the efficient simulation of pass-by noise signals from railway wheels

Downloaded from: https://research.chalmers.se, 2025-12-04 19:51 UTC

Citation for the original published paper (version of record):
Theyssen, J., Deppisch, T., Pieringer, A. et al (2023). On the efficient simulation of pass-by noise signals from railway wheels. Journal of Sound and Vibration, 564.
http://dx.doi.org/10.1016/j.jsv.2023.117889

N.B. When citing this work, cite the original published paper.

research.chalmers.se offers the possibility of retrieving research publications produced at Chalmers University of Technology. It covers all kind of research output: articles, dissertations, conference papers, reports etc. since 2004. research.chalmers.se is administrated and maintained by Chalmers Library

(article starts on next page)

Journal of Sound and Vibration 564 (2023) 117889

Contents lists available at ScienceDirect

Journal of Sound and Vibration

journal homepage: www.elsevier.com/locate/jsvi

On the efficient simulation of pass-by noise signals from railway wheels

Jannik Theyssen *, Thomas Deppisch, Astrid Pieringer, Wolfgang Kropp

Chalmers University of Technology, Division of Applied Acoustics, Department of Architecture and Civil Engineering, Sven Hultins Gata 6, 41258 Gothenburg, Sweden

ARTICLE INFO

Keywords:
Railway wheel
Time domain
Green's functions
Rolling noise
Equivalent sources
Spherical harmonics
BEM
Sound radiation

ABSTRACT

The article presents an approach for calculating pass-by sound pressure radiated from railway wheels in the time domain using moving Green's functions. The Green's functions are obtained by using Finite Element (FE) and Boundary Element (BE) methods in the frequency domain, subsequent inverse Fourier transform, followed by convolution with a time series of rolling contact forces to obtain the pass-by time signals. However, traditional BE methods are computationally expensive due to the low structural damping of the wheel, necessitating a high frequency resolution.

To overcome this issue, a modal approach is introduced in which the pass-by sound radiated by each wheel mode is calculated separately. This approach incorporates the dynamic response of the wheel in the time-domain processing and thus reduces the cost of the BE solution. A modal source signal is introduced to describe the excitation of each mode at each time step. The sound field radiated by unit modal amplitudes is calculated in BE and subsequently approximated by spherical harmonic (SH) equivalent sources, which allows for efficiently calculating acoustic transfer functions for varying relative positions of the wheel and a stationary receiver. Convolution of the source signal with the moving acoustic transfer function produces the pass-by pressure signal.

The article investigates the directivity of the radiation from each mode and finds that most modes, including those with dominant radial deflection, radiate in mostly axial direction at high frequencies. Modes that dominate the pass-by pressure level are identified, both in frequency bands and with respect to the relative positioning of the wheel to the receiver. Finally, it is found that an SH expansion order of approximately 30 is required to satisfy the employed error measures, although lower orders may suffice for an auralisation of the signal.

1. Introduction

Noise emitted from roughness-excited vibrations in the wheels and the track dominates railway noise in a wide range of vehicle velocities. In the higher frequency range starting from about 2 kHz, this rolling noise is typically dominated by the wheel [1]. The upper frequency limit of rolling noise is about 6–8 kHz, higher at larger train speed due to the contact filter [1]. Thus, finding appropriate models to predict the noise radiated from the railway wheels has been an essential part of understanding railway noise. Various modelling approaches have been developed to address this challenge, from analytical models [2] over Rayleigh integral formulations [3] to increasingly elaborate Boundary Element (BE) models [4–9].

* Corresponding author.
E-mail address: jannik.theyssen@chalmers.se (J. Theyssen).

https://doi.org/10.1016/j.jsv.2023.117889
Received 20 February 2023; Received in revised form 15 June 2023; Accepted 19 June 2023
Available online 22 June 2023
0022-460X/© 2023 The Author(s). Published by Elsevier Ltd. This is an open access article under the CC BY license (http://creativecommons.org/licenses/by/4.0/).

Existing models for the radiation from railway wheels generally aim at predicting the sound power, radiation efficiency, and possibly a general approximation of the directivity of the radiated sound. As possible reasons for this, Thompson et al. [7] state that the actual directivity of the wheels is of little relevance in practice since the main interest is averaged sound levels during the pass-by of a train, and the directivity is strongly affected by the local acoustic geometry around the wheel (e.g., the bogie). Further, even when neglecting the local acoustic geometry, modelling the radiation of the complex velocity distribution on the wheel requires a significant computational effort when the radiation up to high frequencies is of interest.

Nevertheless, a lacking description of the directivity can introduce errors in validation measurements carried out in a limited number of discrete positions. Those results will be strongly influenced by the radiation directivity. In addition, the directivity of a moving wheel influences the sound received by a stationary observer. The prediction of the sound pressure in a point on the track side in time domain during a pass-by also gives the possibility to investigate other effects. For example, transients in sound pressure signals due to wheel flats or rail joints are likely not detected in averaged sound levels but can affect the perception of rolling noise by people [10]. To judge the annoyance of such signals, listening tests could facilitate the derivation of psychoacoustic parameters such as impulsiveness or dynamic loudness. Such listening tests in turn require a physically accurate auralisation of the sound received by a stationary observer.

Using a numerical approach as the BEM for creating these time signals requires substantial computational effort for the following reasons:

- As the frequency range of interest reaches up to high frequencies, a high spatial resolution is needed to ensure that at least six elements per wavelength are present.
- The low structural damping of the wheel demands a high frequency resolution to be able to capture the response and radiation around the resonance frequencies of the wheel correctly.
- Calculating pass-by signals that are suitable for psycho-acoustic evaluation requires long time signals with a sufficiently high sampling frequency.

To accomplish this task, the straightforward use of BEM is easily ruled out due to the involved computational effort. Therefore, in the following, the combination of two approaches is presented which allows for calculating pass-by signals through the Fourier series Boundary Element Method (FBEM) [8,11] with reduced computational effort.

Before describing these approaches in detail, the necessary inputs to both approaches are discussed in Section 2, where the simulation model for calculating wheel/rail contact forces during rolling is introduced and the dynamic behaviour of the wheel is described.

The first approach concerns the calculation of the sound radiation from each mode shape of the wheel. Since the derived impulse responses are comparatively short, a rather coarse frequency resolution is sufficient (see Section 3). The second approach is based on the method of equivalent sources. The idea is to represent the sound field caused by each mode shape on the wheel by a set of equivalent sources. In this way, it is possible to calculate the radiated sound pressure in any arbitrary position in a later step without the need to repeat computationally costly FBEM calculations. Here, spherical harmonics (SH) are used as equivalent sources. This is described in Section 4.

In Section 5, a time domain approach is presented to calculate pass-by signals at arbitrary microphone positions. For this, the source signal is created including the contact forces between rail and wheel, the movement of the wheel along the track, and the frequency response of the modes. The contribution of each mode to the pass-by signal is then obtained by convolution of the impulse response functions of the radiation functions based on SHs with the source signal. A summation of all modal contributions gives the final results.

Finally, Section 6 summarises the approach and discusses the results.

2. Rolling contact forces and wheel dynamics

In this article, the WERAN (WhEel/RAil Noise) model [12,13] is used to calculate wheel/rail contact forces during rolling. It combines precalculated impulse response functions for track and wheel with a model for transient rolling contact [12,14]. The rolling contact model is an implementation of Kalker's variational method [14], which is a 3D non-Hertzian model based on the assumption that wheel and rail can be locally approximated by elastic half-spaces. Track and wheel responses are first precalculated as frequency response functions, which are then transformed to impulse response functions via inverse Fourier transform. The track frequency response functions are, in this case, calculated with DIFF [15]. The wheel frequency response function is calculated via modal superposition as described below. The rigid body modes of the wheelset are included when solving the contact problem. The track and wheel responses are then transformed to the time domain via inverse Fourier transform. In this way, the complete dynamics of the wheel and track in the required frequency range are considered in combination with a fully three-dimensional transient and non-linear contact model. This is especially relevant when aiming for auralising transient effects in the rolling contact. WERAN is designed to also include lateral contact forces as a result of friction in the contact [16]. In the following, only vertical forces are taken into account for demonstration of the method. Cheng et al. [9] describe that neglecting the vertical/lateral interaction in the contact patch leads to an overestimation of the contribution of axial modes to the total radiated sound power.

As input data, WERAN requires

- The roughness of the wheel and rail in several parallel lines around the wheel and along the rail,
- the material data and geometries of the wheel and track

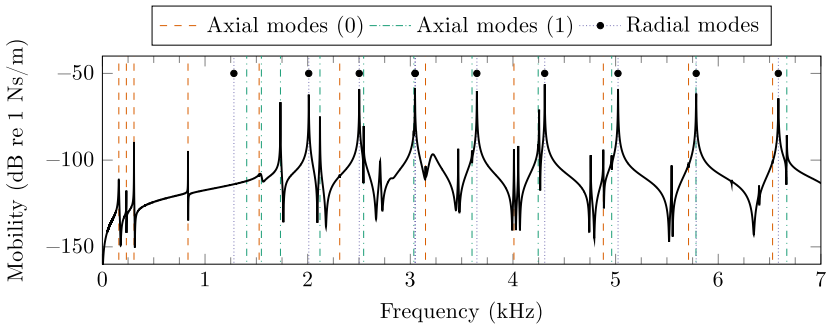

Fig. 1. Driving point mobility for radial excitation at the presumed contact position. The eigenfrequencies of the radial modes and axial modes with 0 and 1 nodal circles are indicated by vertical lines.

- the exact contact geometry and preload as input to the vertical contact model based on Kalker's variational theory [14].

In WERAN, at each discrete time step t_n, the wheel and track impulse response functions are convolved with the contact forces to provide the displacements of both bodies in the contact point as input to the contact model. In the contact model, the vertical contact problem is solved resulting in the vertical contact force $F_c(t_n)$ in the current time step. This force then serves as input to the next convolution step to update the wheel and track displacements. The details of this procedure are described in [17].

The obtained contact forces are then used in a postprocessing step to calculate the vibrations on the complete surface of the wheel and the track, which are in turn input to models for the sound radiation. Here, the focus is however limited to the radiation from the wheel. In addition, the rotation of the wheel is neglected in the prediction of the contact forces and the calculation of the radiated sound field for simplicity. The rotation could however be included with different approaches (see, e.g., [9,18]). The rotation introduces two peaks in the contact point mobility near each eigenfrequency of the wheel. Cheng et al. [9] find that neglecting the rotation leads to an underestimation of the radiated noise by up to 3 dB since in the case of rotation there are twice as many peaks and the apparent damping in the contact is lower.

The velocity $\mathbf{v}(\mathbf{g},\omega)$ at any point $\mathbf{g} = [g_\theta, g_y, g_r]$ on the wheel is based on the superposition of the modes obtained from the WFEM in the form

$$\mathbf{v}(\mathbf{g},\omega) = \sum_l A_l(\omega)\mathbf{\Phi}_l(\mathbf{g}) \tag{1}$$

where $\mathbf{\Phi}_l$ is the mode shape and $\mathbf{\Phi}_l(\mathbf{g})$ is a three element vector that contains the deflection of mode l at position $\mathbf{g}$ in circumferential, axial, and radial direction. The variable $A_l(\omega)$ is the corresponding modal amplitude and ω represents the angular frequency. The modal amplitude is calculated as

$$A_l(\omega) = \mathrm{j}\omega b_l(\omega)\mathbf{F}_e(\omega)\mathbf{\Phi}_l(\mathbf{g}_c)\ , \tag{2}$$

with $\mathbf{g}_c$, the excitation point of the wheel and j, the imaginary unit. The excitation force vector $\mathbf{F}_e(\omega) = [F_\theta(\omega),\ F_y(\omega),\ F_r(\omega)]^{\mathrm{T}}$ is considered a point force acting in position $\mathbf{g}_c$. The term

$$b_l(\omega) = \frac{1}{\Lambda_l(\omega_l^2 - \omega^2 + \mathrm{j}2\omega\omega_l\zeta_l)} \tag{3}$$

describes the frequency-dependent scaling of the modal amplitude due to the dynamic properties of the structure, where ω_l are the eigenfrequencies and ω is the angular frequency. The variable ζ_l represents the damping ratio for mode l. The modal mass Λ_l is calculated as the integral over the whole volume of the body in the form

$$\Lambda_l = \int_V \rho_w \mathbf{\Phi}_l^2 \mathrm{d}V\ , \tag{4}$$

where ρ_w is the density of the steel. The modes are categorised depending on their main direction of motion as radial, axial, or circumferential modes [7]. Depending on the position and direction of excitation, different groups of modes dominate the vibrations. Fig. 1 shows the driving point mobility of the wheel for a radial excitation in the assumed contact position during rolling. The contact position is indicated in Fig. 2.

The wheel geometry is of type BA093 which is, for example, used in the noise measurement vehicle (SMW) of DB Systemtechnik [8]. A reprofiled wheel with a rolling radius of 0.469 m is used. The damping ratios ζ are chosen depending on the number of nodal diameters k according to [1], such that ζ is 10^{-3}, 10^{-2}, and 10^{-4} for $k = 0$, $k = 1$, and $k > 1$, respectively. The mode $(1, 0, r)$ is in practice affected by coupling with the axle and is therefore damped with a damping ratio of 0.95 [1]. When comparing the eigenfrequencies of the wheel in Fig. 1 with the dispersion relation in Fig. 3, it is visible that the main response is due to the radial modes, which are indicated by dots in Fig. 1. However, due to the asymmetric wheel geometry and excitation also axial modes are excited but their amplitudes are lower. Despite the low amplitudes in the case of radial excitation, axial modes are known to be important contributors to the radiated sound of rolling noise [1], which is also shown in the subsequent sections. The coupling

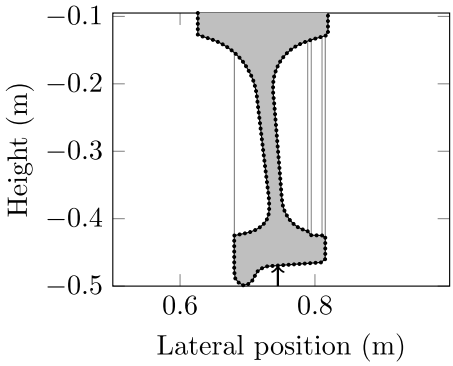

Fig. 2. Lower part of the wheel cross-section. The arrow indicates the location of the contact used in the following.

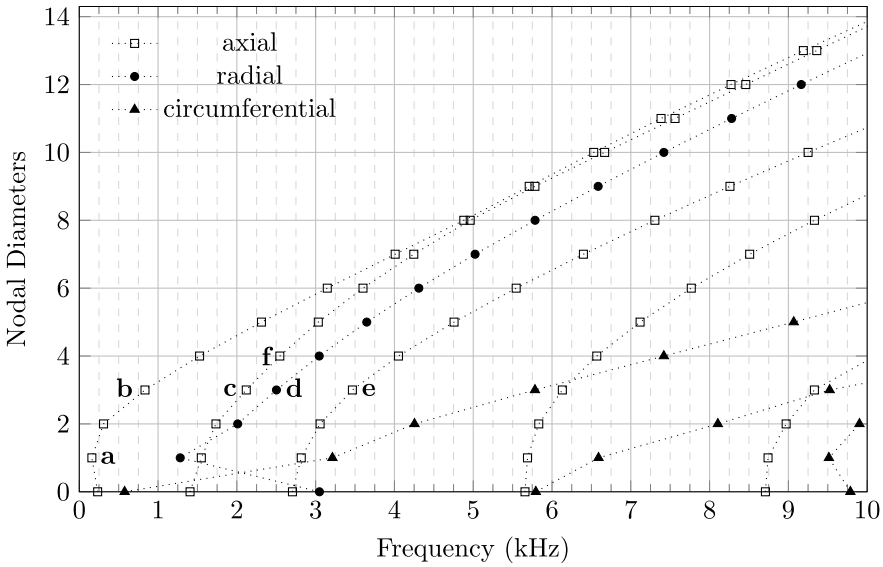

Fig. 3. Dispersion relation of the wheel mode shapes.

between the axial and radial modes is illustrated in Fig. 4, where the radial mode (d) and similarly the axial modes (b), (c), (e), and (f) show a radial displacement on the running surface of the wheel. An interesting question is how significant the impact of each mode in Fig. 3 on pass-by signals is at a given microphone position since beyond the cross-coupling of the axial and radial motion, the excitation and radiation efficiency of each mode are contributing factors. The radiation efficiency of the modes also depends on the modal pattern, i.e., the number of nodal diameters and nodal circles. For instance, it is shown in [7,8] that for typical wheel dimensions, even for five nodal diameters, the radiation efficiency is close to one for frequencies above 1000 Hz. This question is researched in more detail in Section 5.

3. Calculation of the radiated sound from mode shapes

One major obstacle in calculating the radiated sound pressure by means of numerical approaches such as BEM is the required frequency resolution. Due to the highly undamped resonances, the corresponding vibration spectra show sharp maxima which can only be captured by a sufficiently high frequency resolution. Investigating the impulse response of a free wheel shows that a 60 dB decay can reach, or even exceed, 20 s. Capturing 20 s numerically requires a frequency resolution of 1/20 Hz or 0.05 Hz. Calculating spectra up to, e.g., 7 kHz, would thus require solving the BE problem for 140,000 frequency lines. When assuming calculation times of about one minute per frequency line, which might be rather an underestimation for models of this size, the calculation time would be in the order of 100 days. There are a number of attempts to reduce the calculation time, e.g., by adapting the frequency resolution depending on the proximity to a mode. Here, however, a different strategy is developed which avoids the need to calculate

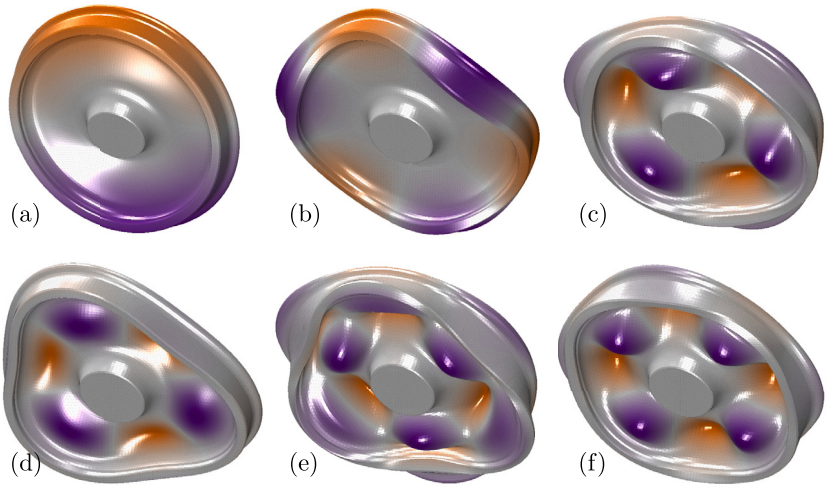

Fig. 4. Vibrational mode shapes: (a): (1, 0, a) at 160 Hz, (b): (3, 0, a) at 834 Hz, (c): (3, 1, a) at 2120 Hz, (d): (3, 0, r) at 2503 Hz, (e): (3, 2, a) at 3467 Hz, (f): (4, 1, a) at 2545 Hz. The colour indicates axial deflection. (For interpretation of the references to colour in this figure legend, the reader is referred to the web version of this article.)

such long impulse responses in BEM altogether by calculating the modal contributions to the pass-by sound pressure separately and including the long dynamic response of the wheel in a source term.

The velocity field on the wheel in Eq. (1) is calculated as the sum of each mode shape $\mathbf{\Phi}_l$ scaled with the corresponding modal amplitude A_l given in Eq. (2). Analogously, the sound field around the wheel is calculated as the sum of the sound radiated from each mode shape $\mathbf{\Phi}_l$ scaled with A_l,

$$p(\mathbf{x}_\mathrm{r}, \omega) = \sum_l A_l(\omega) H_l(\mathbf{x}_\mathrm{r}, \omega) \ . \tag{5}$$

The modal acoustic transfer functions H_l are obtained with a BE model where $A_0\mathbf{\Phi}_l$ is used as input velocity, where $A_0 = 1$ m/s. The complex pressure at a receiver position $\mathbf{x}_\mathrm{r}$ is then calculated for each mode l. Each modal pattern produces a different frequency-dependent pattern in H_l, due to the different relation between the wavelength in the surrounding fluid and the modal pattern on the wheel. It is observable that this frequency-dependent variation is rather smooth. This means that a sparse frequency resolution can be sufficient in the BE calculation, and a subsequent interpolation can achieve the required resolution for the pass-by calculation. Since this interpolation is carried out only after the introduction of equivalent sources in the next step, the 'smoothness' is relevant first there. An example of a several transfer functions H_l is presented in Section 5 below.

4. Equivalent source method

As long as the geometry and position of the wheel and the receiving positions are not changed, the use of the acoustic transfer functions is very efficient. The main disadvantage of the approach is that the transfer functions are only established for a specific set of receiver positions. For a different set of receiver positions, new transfer functions need to be calculated. In the axisymmetric FBEM, the calculation at new receiver positions is very efficient, as long as these new positions have the same radius. However, aiming for the prediction of the sound pressure during a pass-by requires calculating the response along a straight line, involving a continuously changing radius.

To handle arbitrary receiving positions even after having solved the FBEM, a different approach is suggested based on the method of equivalent sources. The equivalent sources method was developed for different practical applications, focusing mainly on the radiation from structures [19–23]. The method is based on the idea of approximating a sound field inside a given volume of interest V (see Fig. 5) by sources q_n placed outside this volume, which must fulfil the given boundary conditions on the surface S. The equivalent sources can be of any source type, i.e., monopole, dipole, multipole sources, or spherical harmonics, as long as they fulfil the given boundary conditions on the surface S. In an equivalent sources approach, the boundary conditions will not be fulfilled exactly over the entire surface S of the radiator but in a least squares sense only. Various approaches have been suggested concerning the choice of the equivalent sources and the approach to determine their amplitudes. For the latter, there are two main approaches in the literature, the collocation method in which the boundary conditions are fulfilled exactly in a discrete number of surface points, or methods minimising the least squares error, in an energy sense, over the surface [22,23].

A set of correctly determined equivalent sources not only describes the pressure field on the surface but also the radiated far-field pressure at any point in the exterior volume V. It is only valid in the far field as the equivalent sources minimise the least squares difference between the velocity of the radiator and the velocity produced by the equivalent sources on the surface. As a consequence,

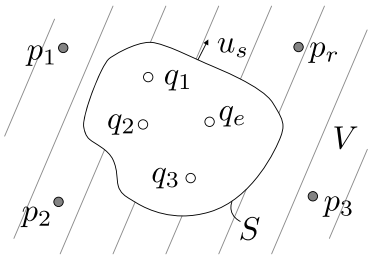

Fig. 5. Receiver points p_n inside the volume V (shaded), and equivalent sources q_n outside of the volume.

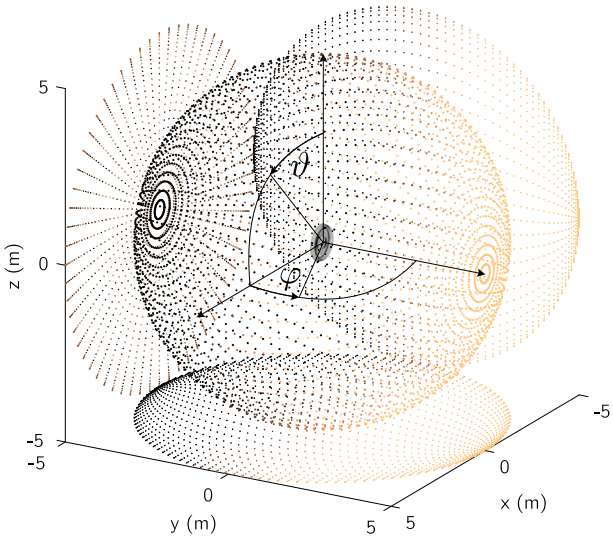

Fig. 6. Position of the wheel and the receiver points on the reference surface S in the FBEM calculation.

the near-field is erroneously reproduced. Observations of the original pressure field in a sufficient number of points in the far field, however, allow for a correct determination of the amplitudes of the equivalent sources.

For I unknown source amplitudes $q_i(\omega)$ and pressure signals $p_m(\omega)$ in M observation points, M has to be equal to or larger than I to avoid an under-determined solution. The propagation between each source and observation point is described by the transfer function $H_{m,i}(\omega)$. The unknown source strengths $\mathbf{q}(\omega)$ are obtained by calculating the inverse of the matrix $\mathbf{H}(\omega)$ and multiplying by the pressure $\mathbf{p}(\omega)$ in the observation points

$$\mathbf{q}(\omega) = [\mathbf{H}(\omega)]^{-1}\mathbf{p}(\omega) \ . \tag{6}$$

Such inverse problems are well known to be ill-posed. Usually, the robustness of such solutions has to be improved by applying some form of regularisation [24].

In the following, the field that is created by the wheel modes is evaluated on a spherical reference surface S in an equiangular grid. The calculations are performed with an FBEM formulation [8]. The equiangular grid allows a convenient export from the cylindrical coordinate system used in FBEM. The wheel is centred at the origin of a 5 m radius sphere as shown in Fig. 6.

The spherical reference surface allows for the sound field to be described in a spherical harmonics (SH) decomposition. Since spherical harmonics (SH) are orthogonal bases, an exact representation of the field is possible given an infinite number of SHs. Order-limited SH representations converge towards the correct solution with increasing order. Alternatively, monopole sources could be used. Such sources lack this orthogonality, but have the advantage that they are comparatively easier to integrate into other BE setups, for example when representing the wheel in a Wavenumber-domain BE formulation [25]. This approach is not followed here.

4.1. Spherical harmonics expansion

The sound pressure field that is radiated by the wheel can be described by a set of SH expansion coefficients. The SHs $Y_n^m(\varphi, \vartheta)$ of order n and degree m are a complete set of orthogonal functions on the sphere and any square-integrable function on the sphere can be expanded in terms of SHs [24, Ch. 6.3.3]. Here, we use a spherical reference surface and thus the SHs can be used as equivalent

sources. The SHs represent the angular part of the solution to the wave equation in spherical coordinates, i.e., they depend on the azimuth angle φ and the zenith angle ϑ. The SH expansion is a multipole expansion, i.e., the zeroth-order SH $Y_0^0(\varphi,\vartheta)$ is a monopole and the first-order SHs $Y_1^{\{-1,0,1\}}(\varphi,\vartheta)$ are dipoles that are aligned with the Cartesian axes. Let us assume that the pressure field $p(\varphi,\vartheta,\omega)$ is known on a spherical observation surface around the wheel, in our case S, and can thus be expanded as a weighted sum of SHs using the complex coefficients $a_n^m(\omega)$,

$$p(\varphi,\vartheta,\omega) = \sum_{n=0}^{\infty}\sum_{m=-n}^{n} a_n^m(\omega) Y_n^m(\varphi,\vartheta) \ . \tag{7}$$

Due to the orthogonality of the SHs, the expansion coefficients $a_n^m(\omega)$ can be obtained by integration over the spherical surface S

$$a_n^m(\omega) = \iint_S Y_n^m(\varphi,\vartheta)^* \ p(\varphi,\vartheta,\omega) \ \mathrm{d}S \ , \tag{8}$$

where $(\cdot)^*$ denotes complex conjugation.

In practice, the sound pressure is obtained numerically and is only available at a discrete set of observation positions on S. Let $\mathbf{p}(\omega)$ be a length-M vector that contains such sound pressures for M observation positions $\{\varphi_{\mathrm{obs}},\vartheta_{\mathrm{obs}}\}$ on S and

$$\mathbf{Y}_N = \begin{bmatrix} Y_0^0(\varphi_1,\vartheta_1) & \dots, & Y_N^N(\varphi_1,\vartheta_1) \\ \vdots & \ddots & \vdots \\ Y_0^0(\varphi_M,\vartheta_M) & \dots, & Y_N^N(\varphi_M,\vartheta_M) \end{bmatrix} \tag{9}$$

an $M\times(N+1)^2$ matrix that contains the SHs up to a maximum order N for the M observation positions. Then, Eq. (7) can be re-expressed with a limited maximum expansion order N

$$\mathbf{p}(\omega) = \mathbf{Y}_N \mathbf{a}_N(\omega) \ , \tag{10}$$

and the least-squares optimal expansion coefficients are obtained as the length-$(N+1)^2$ vector

$$\mathbf{a}_N(\omega) = (\mathbf{Y}_N^{\mathrm{H}}\mathbf{Y}_N)^{-1}\mathbf{Y}_N^{\mathrm{H}} \ \mathbf{p}(\omega) \ , \tag{11}$$

where $(\cdot)^{\mathrm{H}}$ denotes the Hermitian transpose. The limitation to a finite expansion order N creates an error that will be further investigated in the next section. The involved inverse is only well-conditioned if the observation points are regularly distributed on the surface of S and if the orthogonality of the SHs is maintained by choosing a suitable maximum SH order N.

4.2. Determination of the required maximum SH order

Following the approach presented in Section 3, the complex pressure on S is calculated by FBEM for each individual mode, assuming a unit modal amplitude. This produces the acoustic transfer functions H_l, which, in turn, facilitates the calculation of the SH expansion coefficients $a_n^m(\omega)$ for each mode. The equiangular 3600-point grid shown in Fig. 6 is used for the calculation of the expansion coefficients. The maximum SH expansion order $N_{\max}$ is related to a number of uniformly spaced grid points on the sphere by $N_{\max} = \sqrt{M} - 1$, which ensures that Eq. (10) is not under-determined. Because the employed equiangular grid is not uniformly spaced, the robustness of the inversion is investigated by evaluating the condition number of $\mathbf{Y}_N^{\mathrm{H}}\mathbf{Y}_N$ for increasing orders. The matrix is well conditioned up to SH order $N = 29$, so results presented below with $N > 29$ might be numerically inaccurate. The SH order 25 is used for the pass-by prediction. A uniformly distributed grid with 3600 points would facilitate a maximum SH expansion order of up to $N = \sqrt{3600} - 1 = 59$. The SH expansion was implemented using an open-source Matlab library [26].

The expansion coefficients can be used to analyse the directivity of the described wheel. Fig. 7 shows the directivity of the wheel (including all its modes) for a harmonic unit point force excitation with 2250 Hz as obtained by the SH expansion with different maximum expansion orders N. Since this frequency is not an eigenfrequency of the wheel, several mode shapes are excited, which makes the radiation pattern comparatively complex. The directional complexity of the radiation pattern is reduced, and the radiation lobes are broadened when the SH expansion order is reduced. At the same time, the amplitudes are strongly underestimated. This is, however, not visible from Fig. 7, as each individual directivity is normalised by its largest component. For example, the pattern for $N = 3$ would be much smaller than the pattern for $N = 6$ when scaling according to the correct magnitude. For high SH orders, the shape converges as expected. The example is illustrative and the question arises what the required order of the SH is in practical applications, both with respect to the total radiated sound power and to the directivity in the frequency range of interest.

To investigate the sound power, the total pressure is calculated for a harmonic unit force excitation according to Eq. (5). The field on S is then approximated by spherical harmonics as described in the previous section. Fig. 8 shows the radiated sound power in third-octave bands as a function of the order of the SH. It suggests that the radiated sound power can be approximated with $N = 10$ at low frequencies and $N \approx 30$ at medium and high frequencies.

The error in the directivity is here described with a quantity analogous to the modal assurance criterion. Since the compared functions are not mode shapes, the quantity is here called directivity accuracy estimator (DAE) which is calculated as

$$\mathrm{DAE}(\omega) = \frac{\left|\mathbf{p}_{\mathrm{SH}}^{\mathrm{H}}(\omega)\ \mathbf{p}(\omega)\right|^2}{\left(\mathbf{p}^{\mathrm{H}}(\omega)\ \mathbf{p}(\omega)\right)\left(\mathbf{p}_{\mathrm{SH}}^{\mathrm{H}}(\omega)\ \mathbf{p}_{\mathrm{SH}}(\omega)\right)} \ , \tag{12}$$

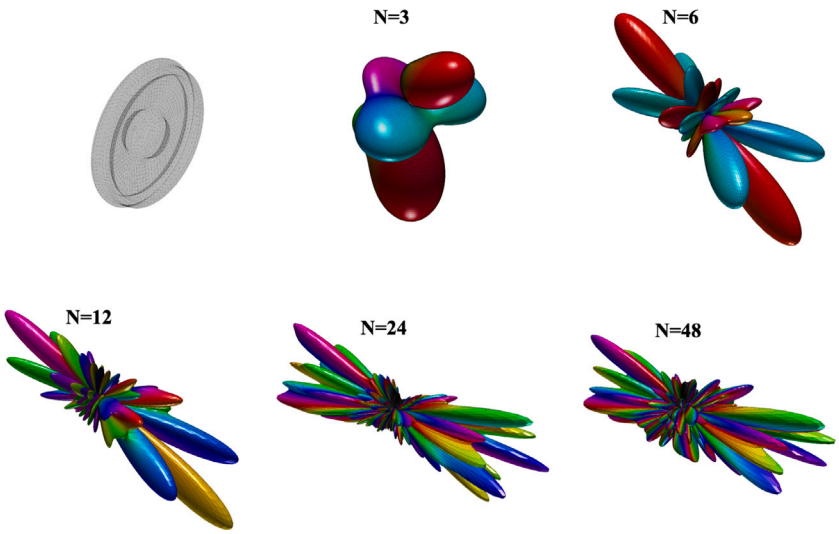

Fig. 7. Orientation and directivity of the wheel at 2250 Hz, obtained with different maximum SH expansion orders N.

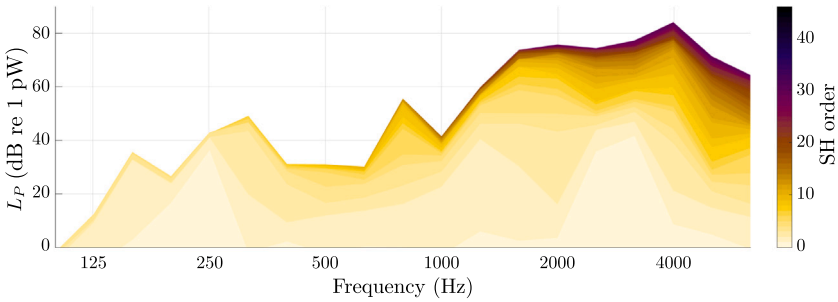

Fig. 8. Predicted sound power in third-octave bands on the 5 m sphere as a function of the SH order.

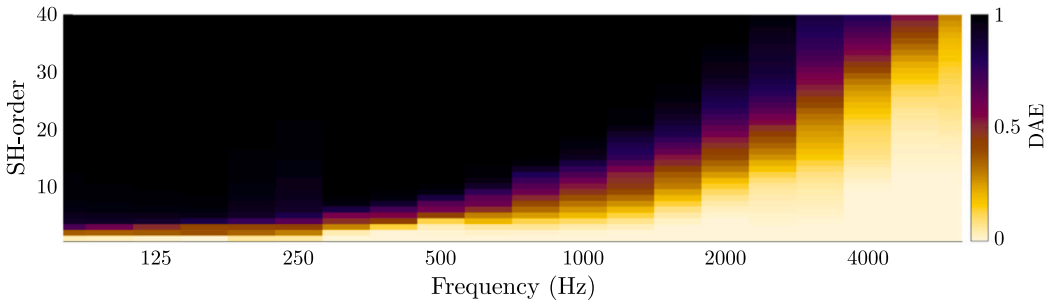

Fig. 9. Directivity accuracy estimator, in 1/3-octave bands, on the 5 m sphere as a function of SH-order.

where $\mathbf{p}_{\mathrm{SH}}(\omega)$ and $\mathbf{p}(\omega)$ are the nodal pressures predicted by SH expansion and FBEM, respectively. The DAE is, similar to the coherence, a measure of the degree of linearity [27]. The formulation here produces a value between 0 and 1, where 1 indicates that the estimate of the pressure vector $\mathbf{p}_{\mathrm{SH}}(\omega)$ is consistent with the original vector $\mathbf{p}(\omega)$.

Fig. 9 shows the DAE for increasing SH orders as an average over each one-third octave band. While for the accurate reproduction of sound power a maximum SH order of approx. 30 is sufficient, in the case of the directivity, this is only true below 4 kHz. However, depending on the application, an SH expansion with a much lower maximum SH order may be sufficient. For instance, in a perceptual

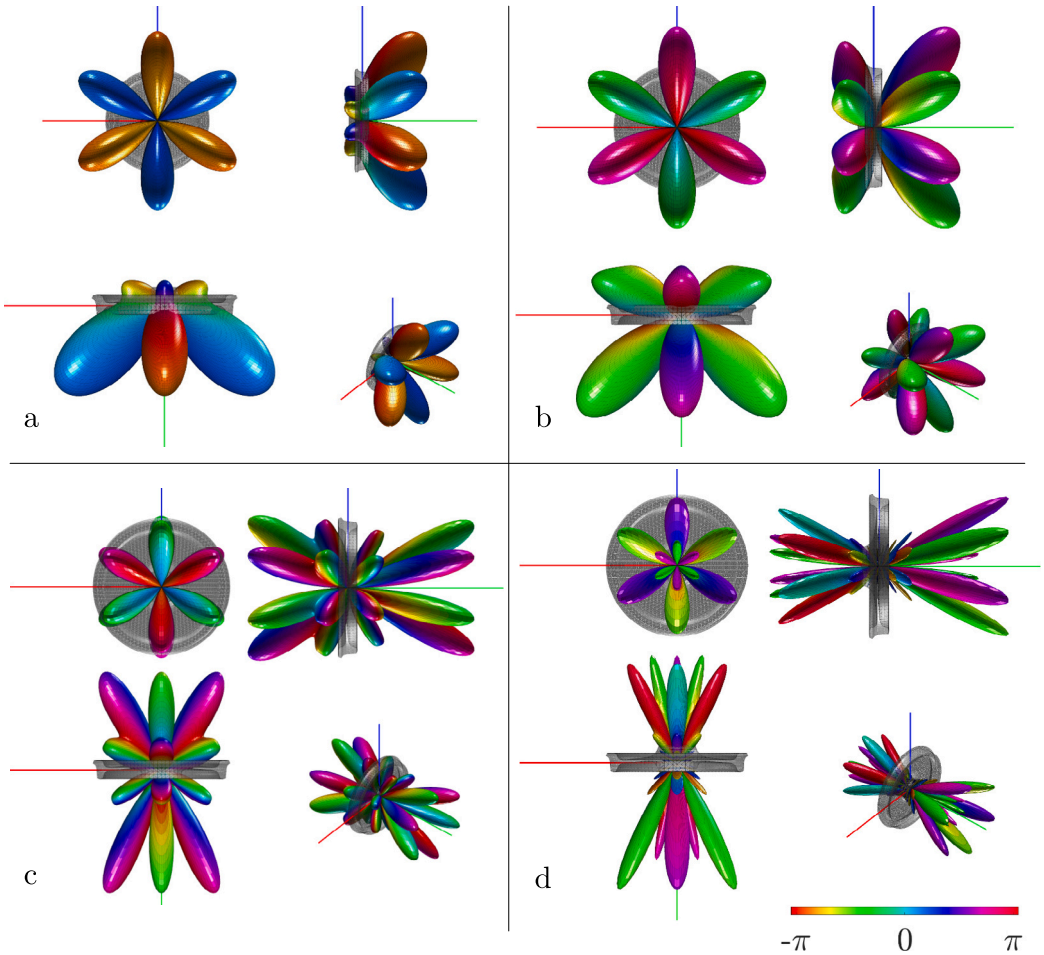

Fig. 10. Directivity of the axial mode $(3, 1, a)$ for (a) 63 Hz, (b) 250 Hz, (c) 1000 Hz, and (d) 4000 Hz. The eigenfrequency of the mode is at 2120 Hz. (For interpretation of the references to colour in this figure legend, the reader is referred to the web version of this article.)

experiment using directional speech and noise sources, a maximum SH order of $N = 5$ was found to be sufficient for auralisation purposes [28]. Using a lower SH order would require adjusting the total sound pressure level accordingly.

4.3. Analysis of the directivity of wheel modes

In the following, the method is used to investigate the directivity of different vibrational modes on the wheel. A few mode shapes were introduced in Fig. 4. The directivities of modes $(3, 1, a)$ and $(3, 0, r)$ (corresponding to (a) and (c) in Fig. 4) are shown in Figs. 10 and 11, respectively. The figures show the directivity pattern of each mode at four different frequencies and from four different perspectives. The size of the shape indicates the magnitude, while the colour indicates the phase. For each frequency, the magnitude is normalised to one. The wheel indicates the orientation of the sound field.

It is visible that the complexity of the directivity pattern increases with increasing frequency. This is expected from the discussion related to Fig. 9. The radiation of the axial mode (3, 1, a) is, at 63 Hz, directed to the one side of the wheel in six main lobes. Due to the asymmetry of the wheel geometry and the resulting vibration pattern, the radiation pattern can also be asymmetric with stronger radiation to one side of the wheel. At high frequencies, the wheel geometry become more influential, leading to additional side lobes. The radiation characteristic of the (3, 0, r) mode in Fig. 11 shows a mostly radial directivity at low frequencies, which transforms into a mostly axial directivity at high frequencies.

5. Simulation of pass-by signals

This section combines the methods presented in the previous sections to simulate the time-domain sound pressure signals at a stationary microphone position $(0, y_0, z_0)$ during the pass-by of a wheel along the track. Fig. 12 shows the corresponding configuration. The receiver is positioned 7.5 m from the track centre, 1.2 m above the rail ($y_0 = 6.75$ m, $z_0 = 0.73$ m).

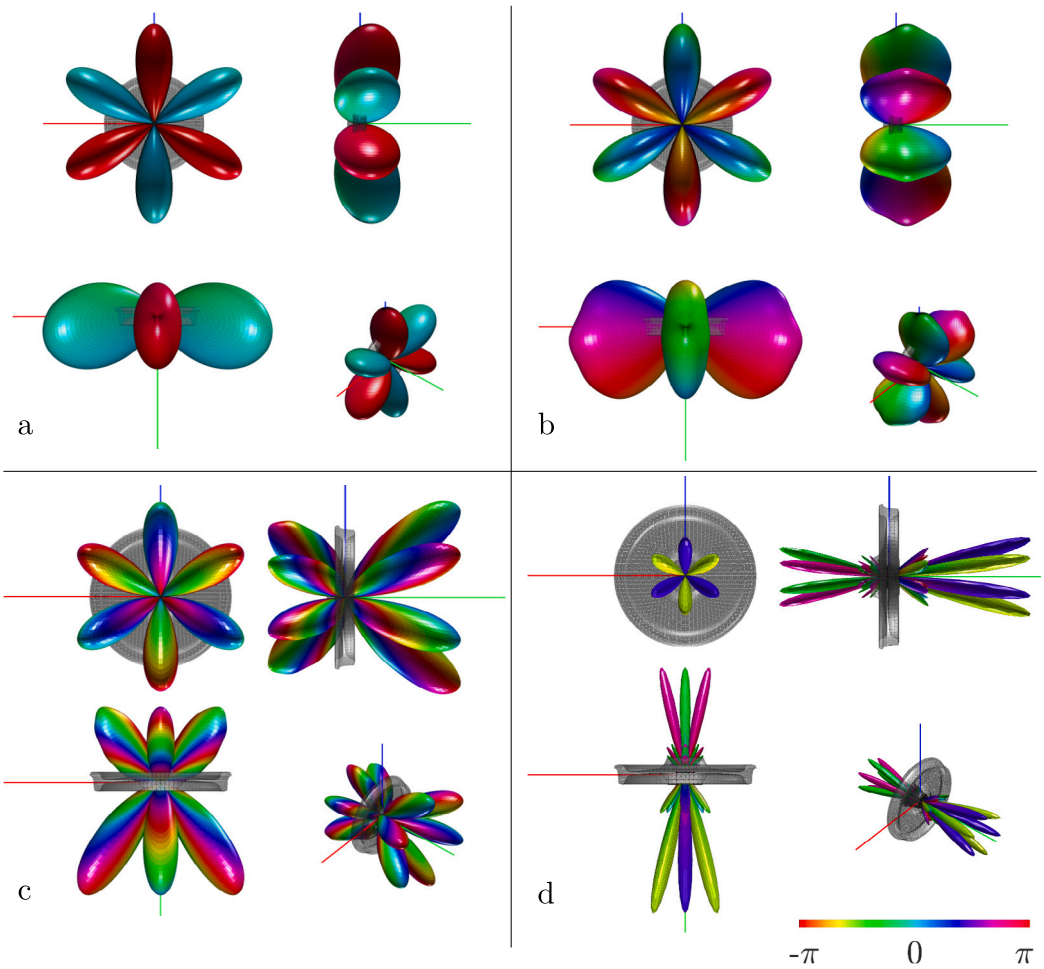

Fig. 11. Directivity of the radial mode $(3, 0, r)$ for (a) 63 Hz, (b) 250 Hz, (c) 1000 Hz, and (d) 4000 Hz. The eigenfrequency of the mode is at 2503 Hz. (For interpretation of the references to colour in this figure legend, the reader is referred to the web version of this article.)

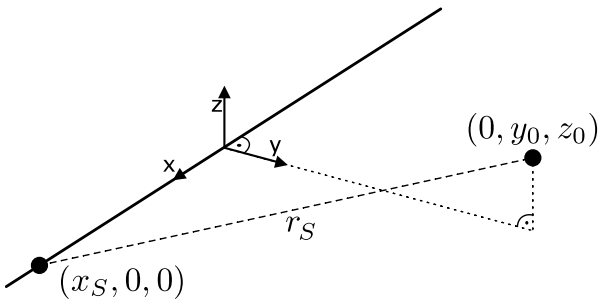

Fig. 12. Axis definition and position of the wheel and stationary microphone. The solid line indicates the trajectory of the wheel.

The calculations are performed separately for each mode and their contributions are summed up at the microphone position in the final step. The computational advantage of this approach is further discussed in Section 6. The involved parts are

- a formulation for the motion of the source,
- the propagation function $h_l(x_S, t)$ for each mode l based on the SH formulation,
- the source signal $q_{S,l}(t)$ based on the contact forces during rolling, and
- the summation of the modal contributions to the total sound pressure in the time domain.

They will be discussed in more detail in the following subsections.

5.1. Description of the motion of the source

A moving source is introduced by changing the source position $(x_S, 0, 0)$ over time t in the form $x_S = vt$, where v is the translational speed of the wheel (here, $v = 100\,\mathrm{km/h}$). At each source position, an acoustic impulse is produced that arrives at the receiver position in the subsequent time. This impulse depends on the relative location of the source and receiver, which is captured in the propagation function h_l introduced in Section 5.2. Due to the moving source, the pressure p_l arriving at the receiver at time t corresponds to the sum of different time instances $t - \tau$, where $\tau \leq t$, in all impulses. This is captured in the convolution of the source signal $q_S(t)$ with the propagation function h_l,

$$p_l(0, y_0, z_0, t) = \int_{-\infty}^{t} q_{S,l}(\tau) h_l(v\tau, t - \tau) \mathrm{d}\tau \ , \tag{13}$$

where the upper limit of the convolution integral is set due to causality requirements, as future source positions should not influence the current sound pressure at the receiver. In a numerical implementation, the integral is replaced by a sum and discrete steps in time and space are considered.

5.2. Propagation function h_l

The propagation function $h_l(x_S, t)$ describes the acoustic transfer from the mode shape to the observer position and is computed as follows. The sound pressure radiated by the mode shape $\mathbf{\Phi}_l$ is approximated by spherical harmonics expansion coefficients as described in Section 4. The expansion coefficients of the pressure field on the reference surface with radius r_0, which encloses the wheel, allow calculating the pressure field on any larger sphere with radius $r > r_0$ using spherical Hankel functions $\mathrm{h}_n(Kr)$ [24, Eq. 6.94],

$$H_l(r_S, \varphi_S, \vartheta_S, \omega) = \sum_{n=0}^{\infty} \frac{\mathrm{h}_n(Kr_S)}{\mathrm{h}_n(Kr_0)} \sum_{m=-n}^{n} a_n^m(\omega)\ Y_n^m(\varphi_S, \vartheta_S) \ , \tag{14}$$

with the wavenumber in air K and

$$\begin{aligned} r_S &= \sqrt{(x_S^2 + y_0^2 + z_0^2)} \ , \\ \varphi_S &= \pi - \arctan\left(\frac{y_0}{x_S}\right) \ , \quad \text{and} \\ \vartheta_S &= \frac{\pi}{2} - \arctan\left(\frac{z_0}{\sqrt{x_S^2 + y_0^2}}\right) . \end{aligned} \tag{15}$$

The modal acoustic propagation function $h_l(x_S, t)$ is then obtained by an inverse Fourier transform of $H_l(r_S, \varphi_S, \vartheta_S, \omega)$, and $h_l(x_S, t < 0) := 0$. Fig. 13 shows an example of the propagation function for mode $(3, 1, a)$ at three different source positions along the track in the frequency ((a) and (b)) and the time domain (c). The spectrum of the transfer functions is rather smooth and can be captured with a frequency resolution of 10 Hz to 20 Hz. The phase of H_l (denoted as $\angle H_l$) is presented in Fig. 13(b) by its derivative with respect to the frequency axis, since the variation is not visible otherwise.

5.3. Source signal

The source signal is calculated using the modal amplitudes $A_l(\omega)$ of the wheel as defined in Eq. (2). Each modal amplitude is divided into two terms $A_l(\omega) = F_{A,l}(\omega) b_l(\omega)$, where $F_{A,l}(\omega)$ represents the excitation

$$F_{A,l}(\omega) = \mathrm{j}\omega \mathbf{F}_e(\omega) \mathbf{\Phi_l}(\mathbf{g_c}) \ , \tag{16}$$

and $b_l(\omega)$ is given in Eq. (3). The excitation force $\mathbf{F}_e$ consists in this case only of the normal contact force F_c, acting radially on the wheel ($\mathbf{F}_e = [0, 0, F_c]^T$). A time series of rolling contact forces has been evaluated in WERAN and is used as an example below. The results produced using this time series are specific to the used input data, including the lateral contact position, the roughness, component geometries, etc., and should not be generalised. A detailed description of the contact force calculation is given in Appendix.

Both $b_l(\omega)$ and $F_{A,l}(\omega)$ have simple time-domain counterparts. The inverse Fourier transform of $F_{A,l}(\omega)$ corresponds to taking the derivative of $\mathbf{F}_e(t)$ with respect to time and scaling with $\mathbf{\Phi}_l(\mathbf{g}_c)$,

$$F_{A,l}(t) = \mathcal{F}^{-1}\left[F_{A,l}(\omega)\right] = \frac{\mathrm{d}}{\mathrm{d}t} \mathbf{F}_e(t) \mathbf{\Phi}_l(\mathbf{g_c}) \ , \tag{17}$$

where $\mathcal{F}^{-1}$ denotes the inverse Fourier transform. An analytical expression of $b_l(\omega)$ in the time domain can be derived as $b_l(\omega)$ describes the frequency response of a simple oscillator whose inverse Fourier transform is

$$b_l(t) = \frac{e^{-2\omega_l \zeta_l t}}{\Lambda_l \omega_l'} \sin(\omega_l' t) \mathrm{H}(t) \ , \tag{18}$$

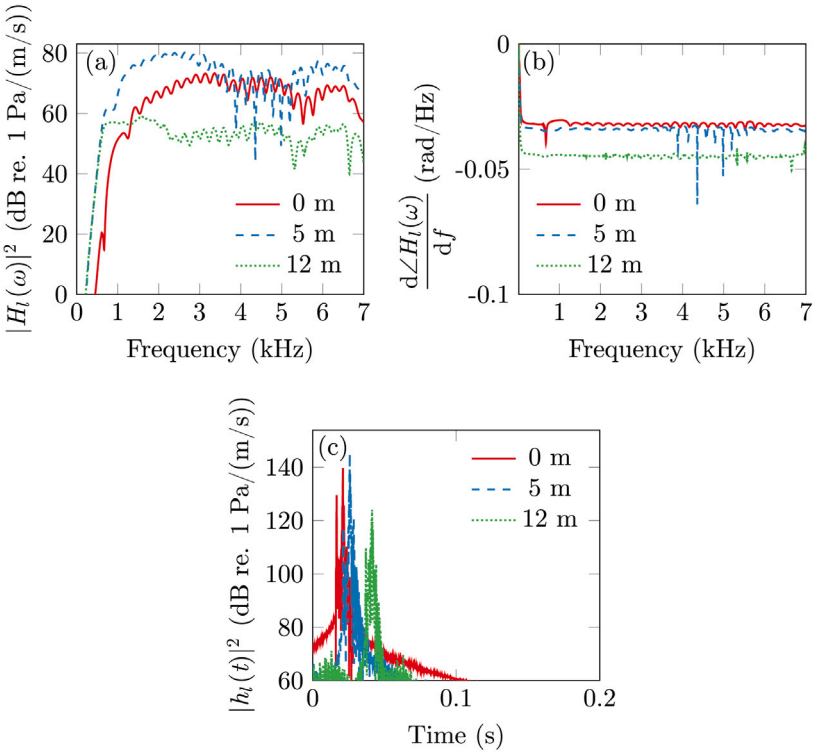

Fig. 13. Acoustic transfer function for mode (3, 1, a). (a): magnitude, (b): change of phase with respect to frequency, (c): modal acoustic propagation function $h_l(t)$.

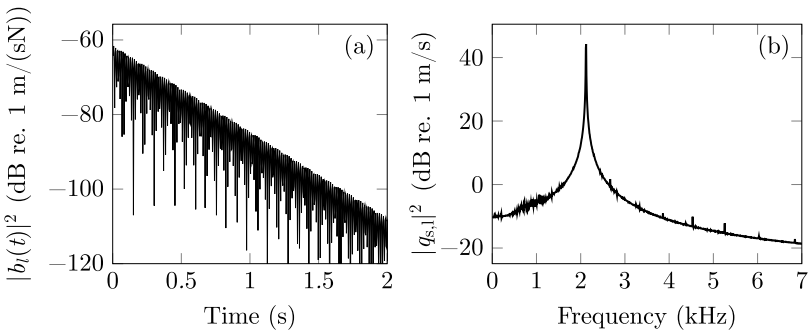

Fig. 14. (a) Impulse response b_l, (b) spectrum of the source signal $q_{S,l}$, both for the mode (3,1,a).

with $\omega_l' = \sqrt{\omega_l^2 - \omega_l^2 \zeta_l^2}$ and the Heaviside step function $\mathrm{H}(t)$. Fig. 14(a) shows the logarithmic decay of $b_l(t)$ for mode (3, 1, a). The source signal $q_{S,l}$ is finally obtained by convolution of the two parts

$$q_{S,l}(t) = \int_{-\infty}^{t} F_{A,l}(\tau)\ b_l(t-\tau)\ \mathrm{d}\tau\ , \tag{19}$$

where the upper limit of the integral is again set due to causality requirements. The spectrum of the source signal is shown in Fig. 14(b).

In the numerical implementation, the convolution integral in Eq. (19) is solved via a sum in N_s discrete time steps of length Δt,

$$q_{S,l}(N_S \Delta t) = \sum_{n=0}^{N_S} F_{A,l}(n\Delta t)\ b_l(N_S \Delta t - n\Delta t)\Delta t\ . \tag{20}$$

This implementation is rather straightforward and requires for each time step one multiplication of the vector b_l with the actual force $F_{A,l}(t)$, an addition of the scaled vector to a register, and a shift of the register for each time step (for example, using the function `circshift` in Matlab).

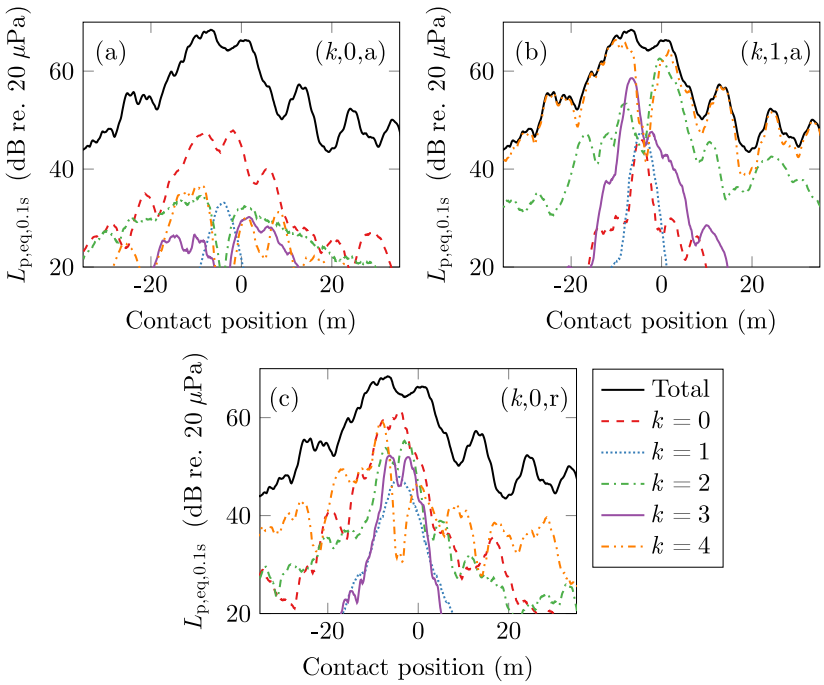

Fig. 15. Contribution of individual modes to the equivalent pressure level averaged over 0.1 s. Axial modes with varying numbers of nodal diameters k, for zero (a) and one (b) nodal circles, and radial modes (c).

5.4. Modal contributions and sum

As the approach is formulated in the time domain, the source signal $q_{S,l}(t)$ is convolved with the propagation function $h_l(x_S, t)$ to obtain the pressure at the microphone due to radiation from the wheel mode. Having created the source signals $q_{S,l}(t)$ and the propagation functions $h_l(x_S, t)$, the time signal at a receiving position can be calculated according to Eq. (13),

$$p(0, y_0, z_0, N_S \Delta t) = \sum_l \sum_{n=0}^{N_S} q_{S,l}(n\Delta t)\ h_l(n\Delta t v, N_S \Delta t - n\Delta t)\Delta t\ , \tag{21}$$

where the inner sum is the sum over all previous wheel positions ($N_S \Delta t v = x_S$) and the outer sum is adding the contribution of all wheel modes. Fig. 15 shows the pass-by levels over wheel position for the total level and the level of the individual modes selected. It indicates that some modes are not relevant for the pass-by signals and could be neglected. Some of the modes are only dominant before and after the pass-by of the wheel, but not when the wheel is located directly in front of the microphone because of their directivity. It also shows that both the axial and the radial modes can be the main contributor to the sound pressure at a receiving position [1].

A different and maybe more complete way to capture the influence of different wheel modes is to look at the total equivalent sound pressure (compare [29, Sec. 3.14]). Here, the signals are averaged over 1 s, corresponding to about 28 m travelling distance of the wheel, which passes by the microphone in the middle of the interval. Similarly to Fig. 3, Fig. 16 shows the dispersion diagram, where the colours of the symbols for the different modes indicate their equivalent sound pressure levels. Only a limited number of modes dominate the total sound pressure level. The modes dominating the sound radiation are axial modes with one and two nodal circles, radial modes and even a circumferential mode. Above 5 to 6 kHz, the modes show a similar influence on the total sound pressure level.

This becomes especially visible when making a sensitivity analysis, which allows for quantifying the effect of removing one mode. Starting from the sound pressure level at the microphone with all modes included, a new level is calculated with the contribution of a single mode removed. Note that only the acoustic contribution is removed, not the influence of the mode on the rolling contact forces (as if introducing a very effective noise shield for a single mode). Fig. 17 shows the change in the equivalent sound pressure level in third-octave bands when the mode that is labelled on the vertical axis is removed. The frequency range can be divided into three areas. At frequencies below 1 kHz, the sound pressure level depends mainly on the modes $(0, 0, a)$, $(2, 0, a)$ and $(1, 0, r)$, each dominating more than one band. In the range between 1 kHz and 2.5 kHz, there are 3 modes ($(2, 1, a)$, $(3, 1, a)$ and $(4, 1, a)$) that dominate the third-octave band which contains their eigenfrequency. Above 2.5 kHz, the impact of the modes on the pass-by level is more evenly distributed between several modes of higher order, both radial and axial, which have their eigenfrequencies in that frequency range.

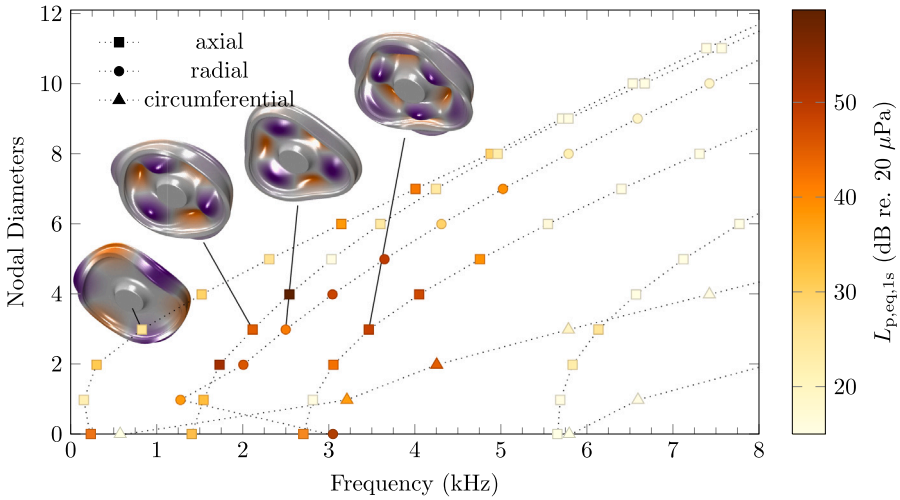

Fig. 16. Contribution of each mode to the 1 s equivalent sound pressure level $L_{p,eq,1s}$.

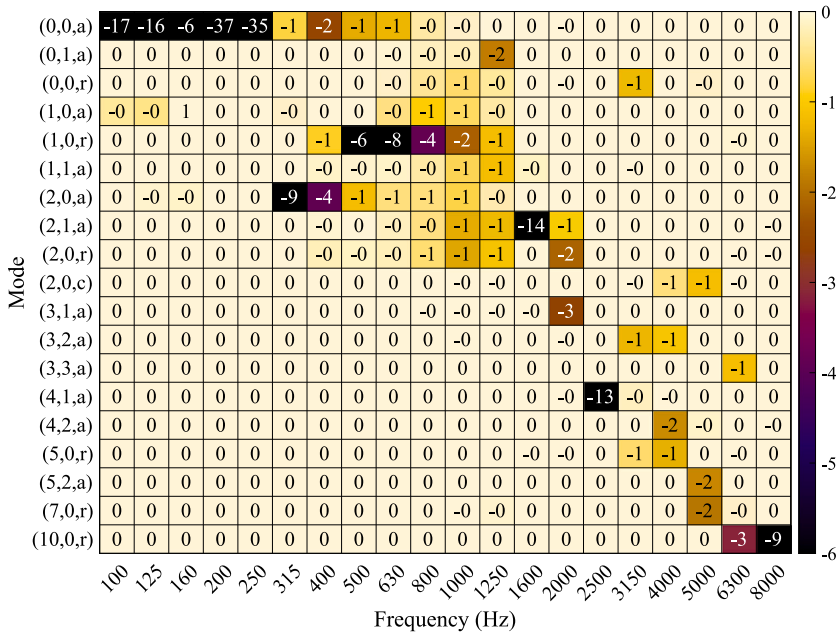

Fig. 17. Effect of removing the contribution of a single mode on the $L_{p,eq,1s}$, in individual 1/3-octave bands in dB (refers to both the numbers and the colour scale). The figure contains only a selection of modes. The modes which have an impact of less than 0.5 dB are not shown.

The wheel modes are orthogonal in their domain, but they are not orthogonal with respect to sound radiation during the pass-by. This means that modes can interact in an energetic sense in terms of the radiated sound power. In this way, a strong variation in the sound pressure level when one mode is removed (see Fig. 17), does not necessarily imply that this mode is the strongest contributor to the pass-by pressure level.

However, when presenting the pass-by as a spectrogram in Fig. 18, it becomes obvious that single modes dominate the signal in a certain frequency range. For example, two modes that are dominant in their respective third-octave bands in Fig. 17 clearly produce large pass-by pressure levels.

The third-octave band spectrum of the 1 s averaged, total pass-by pressure $L_{p,eq,1s}$ is shown in Fig. 19. The highest sound pressure levels are found in the frequency range between 1.6 kHz and 5 kHz, with the maximum in the 2.5 kHz band which is dominated by the mode $(4, 1, a)$.

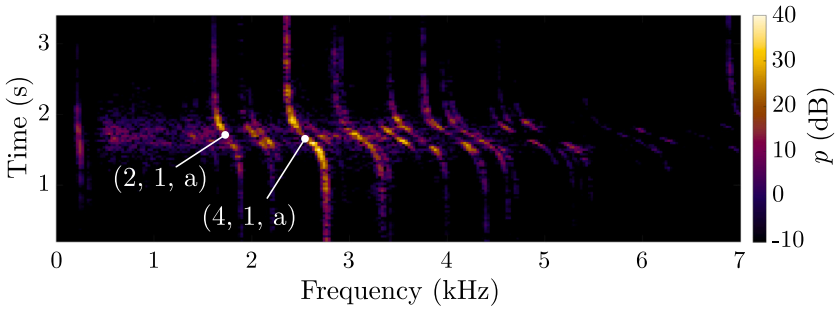

Fig. 18. Spectrogram of the pass-by sound pressure at a stationary microphone position. Individual modes can be identified.

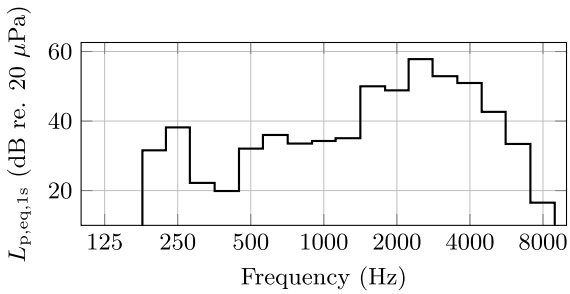

Fig. 19. Spectrum of $L_{\mathrm{p,eq,1s}}$ in third-octave bands.

6. Discussion

This section discusses computational efficiency and limitations in the presented method. This presented approach has a distinct computational advantage compared to a more conventional BE approach, which would calculate the sound radiation from the force-excited vibrating wheel. While this conventional approach would not require calculating the transfer functions for each individual mode, the required high frequency resolution still leads to about 4–15 times more calculations than in the proposed approach.[1] Further, each of these calculations is computationally more costly due to the larger number of receiver points (e.g., 50 000 points for a 1 mm discretisation of a 50 m track section compared to 60 points on the half-circle). On top of that, the proposed modular approach allows for modifying the contact forces, excitation positions and microphone positions without the need to re-calculate the acoustic transfer functions with FBEM. There is additional potential in omitting modes that do not significantly contribute to the total sound pressure, which is not factored in here.

The calculation of the acoustic transfer functions was carried out for a wheel with a clamped boundary condition at the hub. It was observed that the mode shapes of the wheel are similar to those of a wheel in a complete wheelset. The difference is considered small compared to other errors introduced by, for example, neglecting the reflections at the bogie and the vehicle underbody. Since the effect of the suspension is important for predicting the rolling contact forces in the lower frequency range, the prediction in WERAN includes the rigid body modes of the wheelset and a suspension.

So far, the approach has been implemented for the radiation of the wheel into free space. However, it may be extended to include reflections from the ground and other surrounding surfaces such as the floor of the wagon. To include this, one might rather use a BEM than FBEM approach for the calculation of the acoustic transfer functions, as the additional geometrical features might be more conveniently included in Cartesian rather than cylindrical coordinates.

The proposed method can be extended to include a complete wheelset in both vibration and radiation prediction. Further extension can involve the rotation of the wheel or wheelset.

7. Conclusion

This article proposes a computationally efficient method to calculate pass-by signals from railway wheels. It was found that the proposed modal approach for calculating the sound radiation has computational advantages for time-domain models compared to a standard BE approach. The advantage is gained by carrying out the numerically intensive, frequency-domain BE calculations with a sparse frequency resolution and including the dynamic response of the wheel in a modal source strength in the subsequent

[1] Depending on the included number of modes and relative frequency resolution. For 50 modes, which each need to be calculated with 20 Hz resolution instead of 0.05 Hz, the factor is 20 Hz/0.05 Hz/50 = 8.

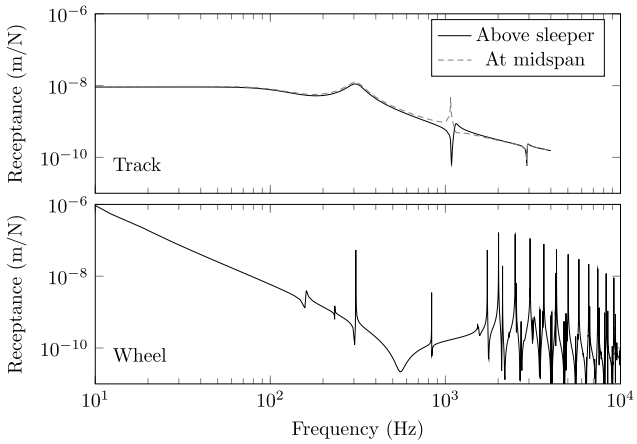

Fig. A.20. Top: Point receptances of the track for excitation above a sleeper and at midspan. Bottom: radial point mobility of the wheel.

time domain noise prediction. The modal approach allows for the analysis of various modal contributions. It was found that, for this specific example, the modes $(0, 0, a)$, $(2, 0, a)$, and $(1, 0, r)$ dominate the sound pressure level below 1 kHz. The modes ($(2, 1, a)$, $(3, 1, a)$, $(2, 0, r)$ and $(4, 1, a)$) dominate the third-octave bands which contain their respective eigenfrequency up to 2.5 kHz. For higher frequencies, the contribution is shared among several higher modes. These findings agree with what is stated in literature [1]. The directivity of individual modes was investigated. The complexity of the directivity pattern increases with frequency. At high frequencies, the main radiation direction is axial, even for radial modes. Due to this complex directivity, during the pass-by, different modes dominate the total sound pressure level, depending on the position of the wheel in relation to the receiver. Following the numerical investigations, a maximum SH expansion order of approximately 30 or higher is found to be required to satisfy the employed error measures. However, depending on the application, much lower SH orders might be sufficient.

CRediT authorship contribution statement

Jannik Theyssen: Conceptualization, Methodology, Software, Investigation, Writing – original draft, Writing – review & editing, Visualization. **Thomas Deppisch:** Methodology, Software, Writing – original draft. **Astrid Pieringer:** Software, Writing – review & editing, Funding acquisition. **Wolfgang Kropp:** Conceptualization, Methodology, Writing – original draft, Supervision, Funding acquisition.

Declaration of competing interest

The authors declare that they have no known competing financial interests or personal relationships that could have appeared to influence the work reported in this paper.

Data availability

Data will be made available on request

Acknowledgements

The current study is part of the ongoing activities in CHARMEC — Chalmers Railway Mechanics (www.charmec.chalmers.se). Parts of the study have been funded from the European Union's Horizon 2020 research and innovation programme in the In2Track3 project under grant agreements No 101012456. The computations were enabled by resources provided by the Swedish National Infrastructure for Computing (SNIC), partially funded by the Swedish Research Council through grant agreement no. 2018-05973.

Appendix. Description of the rolling contact force calculation

A time series of contact forces is calculated with WERAN [16] assuming a track consisting of rails with profile UIC60 E2 on monobloc concrete sleepers in ballast modelled with finite elements in DIFF [15]. Fig. A.20 presents the vertical track point receptance above a sleeper and at midspan between two sleepers. The track parameters are listed in [30]. The figure also shows the radial point receptance on the wheel running band. The rigid body modes of the wheelset have been included in the wheel model for the prediction of the contact forces. The rail roughness used has been measured at the highspeed line Munich–Augsburg in Germany [31]. The wheel roughness originates from a wheel with composite brake blocks on a French freight train [32]. These

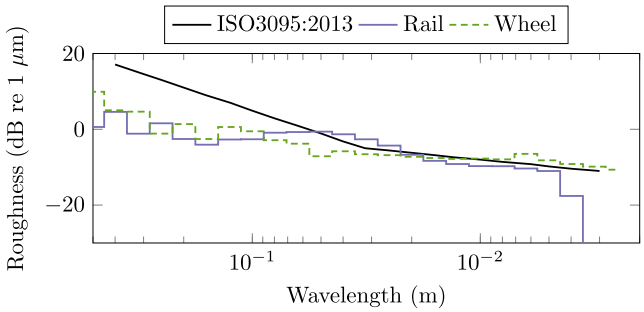

Fig. A.21. Roughness in the running band of the wheel and the rail.

roughnesses, each measured in several parallel lines, are interpolated laterally to produce 21 evenly spaced parallel lines in the contact area. More details of the roughness processing are given in [30]. The combined wheel/rail roughness provides the excitation of the wheel/rail system during rolling. The averaged 1/3-octave band spectra of both the wheel and the rail roughness are given in Fig. A.21 in comparison to the ISO 3095: 2013 limit for the rail roughness applied during vehicle type testing [29]. The velocity v is set to 100 km/h. Although the simulation model WERAN can include wheel rotation, this is not considered here. The wheel does not rotate and the position $\mathbf{g}_c$ is fixed.

References

[1] D.J. Thompson, Railway Noise and Vibration: Mechanisms, Modelling and Means of Control, first ed., Elsevier, Amsterdam, Boston, 2009.

[2] P. Remington, Wheel/rail noise— part I: Characterization of the wheel/rail dynamic system, JSV 46 (3) (1976) 359–379, http://dx.doi.org/10.1016/0022-460X(76)90861-0.

[3] E. Schneider, K. Popp, H. Irretier, Noise generation in railway wheels due to rail-wheel contact forces, JSV 120 (2) (1988) 227–244, http://dx.doi.org/10.1016/0022-460X(88)90431-2.

[4] U. Fingberg, Ein modell für das kurvenquietschen von schienenfahrzeugen (A model for the curve squeal of rail vehicles), in: VDI Fortschrittberichte, Vol. 140, 1990.

[5] D.J. Thompson, Wheel-rail noise generation, part II: Wheel vibration, JSV 161 (3) (1993) 401–419, http://dx.doi.org/10.1006/jsvi.1993.1083.

[6] A.H.W.M. Kuijpers, G. Verbeek, J.W. Verheij, An improved acoustic Fourier boundary element method formulation using fast Fourier transform integration, JASA 102 (3) (1997) 1394–1401, http://dx.doi.org/10.1121/1.420099.

[7] D. Thompson, C. Jones, Sound radiation from a vibrating railway wheel, JSV 253 (2) (2002) 401–419, http://dx.doi.org/10.1006/jsvi.2001.4061.

[8] F. Fabre, J.S. Theyssen, A. Pieringer, W. Kropp, Sound radiation from railway wheels including ground reflections: A half-space formulation for the fourier boundary element method, JSV 493 (2021) 115822, http://dx.doi.org/10.1006/jsvi.2001.4061.

[9] G. Cheng, Y. He, J. Han, X. Sheng, D. Thompson, An investigation into the effects of modelling assumptions on sound power radiated froma high-speed train wheelset, JSV 495 (2021) 115910, http://dx.doi.org/10.1016/j.jsv.2020.115910.

[10] J.C.O. Nielsen, A. Pieringer, D.J. Thompson, P.T. Torstensson, Wheel–rail impact loads, noise and vibration: A review of excitation mechanisms, prediction methods and mitigation measures, in: G. Degrande, G. Lombaert, D. Anderson, P. de Vos, P.-E. Gautier, M. Iida, J.T. Nelson, J.C.O. Nielsen, D.J. Thompson, T. Tielkes, D.A. Towers (Eds.), Noise and Vibration Mitigation for Rail Transportation Systems, Vol. 150, in: Notes on Numerical Fluid Mechanics and Multidisciplinary Design, Springer International Publishing, Cham, 2021, pp. 3–40, http://dx.doi.org/10.1007/978-3-030-70289-2_1.

[11] S. Finnveden, M. Fraggstedt, Waveguide finite elements for curved structures, JSV 312 (4–5) (2008) 644–671, http://dx.doi.org/10.1016/j.jsv.2007.11.020.

[12] A. Pieringer, W. Kropp, D.J. Thompson, Investigation of the dynamic contact filter effect in vertical wheel/rail interaction using a 2D and a 3D non-hertzian contact model, Wear 271 (2011) 328–338, http://dx.doi.org/10.1016/j.wear.2010.10.029.

[13] A. Pieringer, W. Kropp, J. Nielsen, The influence of contact modelling on simulated wheel/rail interaction due to wheel flats, Wear 314 (1–2) (2014) 273–281, http://dx.doi.org/10.1016/j.wear.2013.12.005.

[14] J.J. Kalker, Three-Dimensional Elastic Bodies in Rolling Contact, 2 of Solid Mechanics and Its Applications, Springer Netherlands, Dordrecht, 1990.

[15] J. Nielsen, A. Igeland, Vertical dynamic interaction between train and track – influence of wheel and track imperfections, JSV 187 (5) (1995) 825–839, http://dx.doi.org/10.1006/jsvi.1995.0566.

[16] A. Pieringer, A numerical investigation of curve squeal in the case of constant wheel/rail friction, JSV 333 (18) (2014) 4295–4313, http://dx.doi.org/10.1016/j.jsv.2014.04.024.

[17] A. Pieringer, Time-Domain Modelling of High-Frequency Wheel/Rail Interaction (Doctoral thesis), Chalmers University of Technology, 2011.

[18] A. Pieringer, L. Baeza, W. Kropp, Modelling of railway curve squeal including effects of wheel rotation, in: J.C. Nielsen, D. Anderson, P.-E. Gautier, M. Iida, J.T. Nelson, D. Thompson, T. Tielkes, D.A. Towers, P. de Vos (Eds.), Noise and Vibration Mitigation for Rail Transportation Systems, Vol. 126, in: Notes on Numerical Fluid Mechanics and Multidisciplinary Design, Springer Berlin Heidelberg, Berlin, Heidelberg, 2015, pp. 417–424, http://dx.doi.org/10.1007/978-3-662-44832-8_50.

[19] v.L. Cremer, M. Wang, Die synthese eines von einem beliebigen Körper in luft erzeugten feldes aus kugelschallfeldern und deren realisierung in durchrechnung und experiment (synthesis of spherical wave fields to generate the sound radiated from bodies of arbitrary shape, its realization by calculation and experiment), Acustica 65 (2) (1988) 53–74.

[20] G.H. Koopmann, L. Song, J.B. Fahnline, A method for computing acoustic fields based on the principle of wave superposition, JASA 86 (6) (1989) 2433–2438, http://dx.doi.org/10.1121/1.398450.

[21] M. Heckl, Bemerkung zur berechnung der schallabstrahlung nach der methode der kugelfeldsynthese (Remarks on the calculation of sound radiation using the method of spherical wave synthesis), Acta Acust. 68 (4) (1989) 251–257.

[22] M. Ochmann, Die multipolstrahlersynthese – ein effektives verfahren zur berechnung der schallabstrahlung von schwingenden strukturen beliebiger oberflächengestalt (the multipole synthesis - an effective method for calculating the sound radiation from vibrating structures of arbitrary surface shape), Acta Acust. 72 (4) (1990) 233–246.

[23] R. Jeans, I.C. Mathews, The wave superposition method as a robust technique for computing acoustic fields, JASA 92 (2) (1992) 1156–1166, http://dx.doi.org/10.1121/1.404042.
[24] E.G. Williams, Fourier Acoustics: Sound Radiation and Nearfield Acoustical Holography, Academic Press, 1999.
[25] H. Li, D. Thompson, G. Squicciarini, X. Liu, M. Rissmann, F.D. Denia, J. Giner-Navarro, Using a 2.5D boundary element model to predict the sound distribution on train external surfaces due to rolling noise, JSV 486 (2020) 115599, http://dx.doi.org/10.1016/j.jsv.2020.115599.
[26] A. Politis, Microphone Array Processing for Parametric Spatial Audio Techniques (Doctoral thesis), Aalto University, 2016.
[27] R.J. Allemang, The modal assurance criterion – twenty years of use and abuse, Sound Vib. 37 (8) (2003) 14–23.
[28] M. Frank, M. Brandner, Perceptual evaluation of spatial resolution in directivity patterns, in: Proc. of the German Annual Conference on Acoustics, DAGA, 2019.
[29] ISO 3095:2013, Acoustics — Railway Applications — Measurement of Noise Emitted By Railbound Vehicles, Standard, International Organization for Standardization, 2013.
[30] A. Pieringer, W. Kropp, Model-based estimation of rail roughness from axle box acceleration, Appl. Acust. 193 (2022) 108760, http://dx.doi.org/10.1016/j.apacoust.2022.108760.
[31] D. Thompson, G. Squicciarini, J. Zhang, I. Lopez Arteaga, E. Zea, M. Dittrich, E. Jansen, K. Arcas, E. Cierco, F. Magrans, A. Malkoun, E. Iturritxa, A. Guiral, M. Stangl, G. Schleinzer, B. Martin Lopez, C. Chaufour, J. Wändell, Assessment of measurement-based methods for separating wheel and track contributions to railway rolling noise, Appl. Acust. 140 (2018) 48–62, http://dx.doi.org/10.1016/j.apacoust.2018.05.012.
[32] V. Delavaud, Modélisation Temporelle de L'Interaction Roue/Rail Pour Une Application Au Bruit de Roulement Ferroviaire (Doctoral thesis), ENSTA ParisTech, 2011.